Materials Chemistry and Physics 140 (2013) 183–190

Contents lists available at SciVerse ScienceDirect

Materials Chemistry and Physics

journal homepage: www.elsevier.com/locate/matchemphys

Tension–tension fatigue behavior of layer-to-layer 3-D angle-interlock woven composites

Limin Jin [a], Bo Cheng Jin [b], Nikhil Kar [b], Steven Nutt [b], Baozhong Sun [a], Bohong Gu [a,*]

[a] College of Textiles, Key Laboratory of High-performance Fibers & Products, Ministry of Education, Donghua University, Shanghai 201620, China
[b] Gill Composites Center, Department of Chemical Engineering and Materials Science, University of Southern California, Los Angeles, CA 90089, USA

HIGHLIGHTS

- Acoustic emission and FEA model were used to characterize fatigue damage.
- Three fatigue life ranges with different damage modes were found.
- The 3D woven structure will influence the fatigue damage significantly.

ARTICLE INFO

Article history:
Received 19 October 2012
Accepted 8 March 2013

Keywords:
Composite materials
Fatigue
Microstructure
Finite element analysis

ABSTRACT

The tension–tension fatigue behavior of (the layer-to-layer) three-dimensional angle-interlock woven composite (3DAWC) was investigated using the acoustic emission (AE) technique, examination of damaged regions via light microscopy and micro-CT, and finite element analysis (FEA). AE events occurred during the entire fatigue process, and damage modes were determined based on cumulative fatigue damage of the 3DAWC undergoing tension-tension cyclic loading. FEA was employed to determine stress distribution and specific regions of stress concentrations within the composite structure. Debonding occurred at the warp tow-matrix-weft tow interface where the warp tows exhibited a maximum in amplitude of undulation. In addition, interrupted tests were performed to investigate fatigue damage modes of the 3DAWC at specific points in the fatigue life. Fatigue damage occurred in three distinct stages with characteristic damage modes.

1. Introduction

Three-dimensional (3D) textile structural composites (3DTSCs) are currently being used in structural engineering applications due to their high delamination resistance and fracture toughness [1]. These materials are manufactured with various complex 3D reinforcements such as woven, braided and knitted fabrics. One example of such 3D materials is the 3D angle-interlock woven composites (3DAWCs), which feature attractive properties and are readily processed using a traditional dobby loom or a jacquard loom. In angle-interlock weaving, yarns or tows are placed at an angle to the thickness direction, thereby interlocking adjacent plies. 3D angle-interlock woven fabrics (3DAWFs) can be classified as either layer-to-layer angle-interlock (undulated warp tows enter one or more layers of straight weft tows), or through-thickness angle-interlock (undulated warp tows go through all layers of straight weft tows) woven fabrics [2–4]. Such weaving structures impart damage tolerance and energy dissipation performance along the thickness direction. These enhancements and the potential engineering applications motivate much of the present research on the mechanical properties of 3DAWCs.

Investigations of the mechanical behavior of 3DAWCs have often been coupled with computational or analytical modeling. And most of the researches are focus on the basic mechanical properties in tension and compression [5–11]. In addition, because of the enhanced resistance to delamination resistance imparted by the undulated warp tows along the thickness direction, 3DAWCs have been considered for high-velocity impact protection, and ballistic penetration tests have been performed to explore mechanisms of damage and failure [12–14]. Moreover, considering the wide range of potential applications for the 3DAWCs, understanding fatigue behavior and the primary mechanisms responsible to fatigue failure are of critical importance. Tsai et al. [15] conducted a comparative study on the tensile fatigue behavior of three-layer and five-layer 3DAWC plates. The fatigue damage mechanisms primarily involved transverse cracks in the warp tows, debonding between

* Corresponding author. Tel.: +86 21 67792661; fax: +86 21 67792627.
E-mail address: gubh@dhu.edu.cn (B. Gu).

0254-0584/$ – see front matter © 2013 Elsevier B.V. All rights reserved.
http://dx.doi.org/10.1016/j.matchemphys.2013.03.020

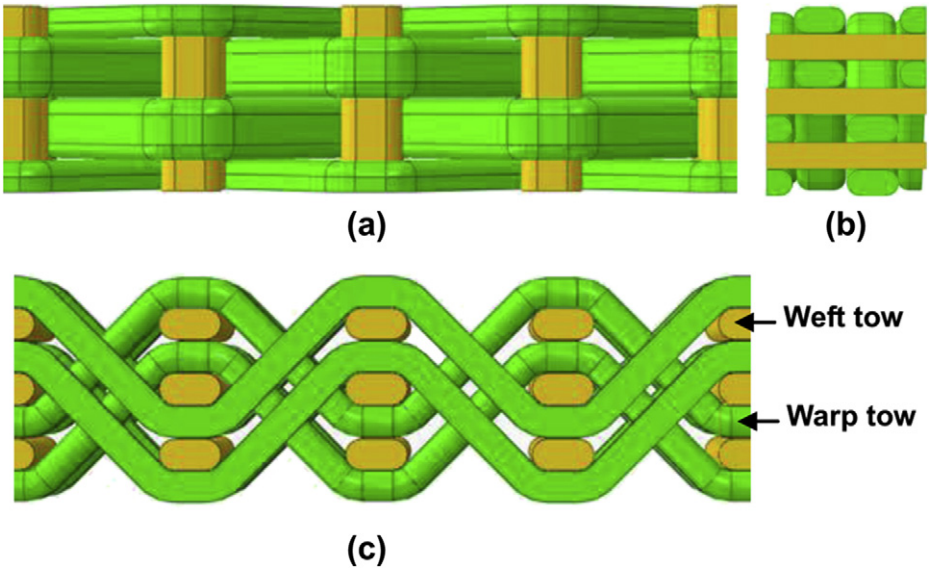

Fig. 1. Layer-to-layer angle-interlock structure. (a) Top view; (b) side view; (c) front view.

Table 1
Specifications of 3DAWF.

Tows	Fiber type	Linear density (Tex)	Density (ends/cm)	Layers
Warp	Glass fiber	480 × 2	11	
Weft	Glass fiber	480 × 1	2	6

the warp and weft tows, debonding extension and deflection into the matrix, and weft tows breakages. Gowayed et al. [16] developed a model to analyze the fatigue behavior and life of fiber/epoxy 3DAWC. More recently, Jin et al [17] studied three-point bending fatigue of a layer-to-layer 3DAWC and reported that the integrated construction structure resisted delamination under high-cycle fatigue conditions. There have been few reports of the tension-tension fatigue behavior of 3DAWCs.

In this paper, we investigate damage and failure of a layer-to-layer 3DAWCs subjected to tension-tension fatigue loading. S–N curves are measured, displacement variations and acoustic emission (AE) events are monitored during the entire fatigue process. Tests were also interrupted at specific stages in the fatigue life to determine mechanisms and modes of damage during tension–tension cyclic loading. In addition, finite element analysis (FEA) is employed to determine stress distribution and specific regions of stress concentration within this composite structure under tension-tension fatigue loading.

2. Experimental

2.1. Materials

In the layer-to-layer 3DAWF, the undulated warp tows interlaced the non-crimp weft tows to form a stable and integrated woven construction, as shown in Fig. 1. All the warp and weft tows were made of glass fiber. Table 1 lists the specifications of the 3DAWF.

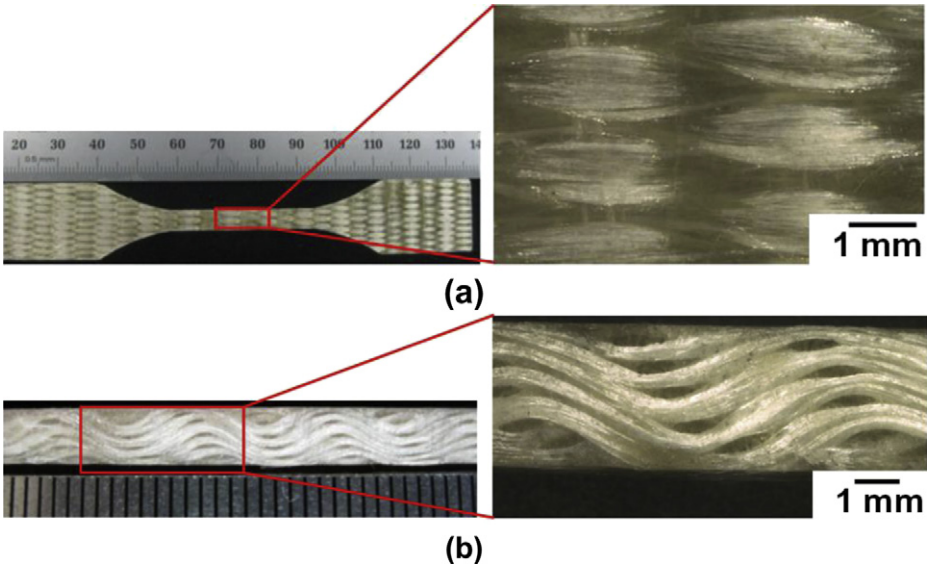

Fig. 2. 3DAWC sample. (a) Surface; (b) cross-section.

Table 2
Specifications of glass fiber and resin.

	Type	*E* (GPa)	Poisson's ratio	Density (g cm^{-3})
Warp/weft tow	Glass fiber	70	0.2	1.44
Matrix	Resin	3.65	0.35	1.36

Vacuum assisted resin transfer molding (VARTM) was employed to manufacture the 3DAWC plate. The polyester resin (AROPOL™ INF 80501-50, Ashland Composite Polymers, China) had a viscosity of 0.18Pas at 25°C, and the proportion of resin to curing agent (AKZO® M-50) was 100:1 by weight. The resin solution was injected into the 3DAWF, then cured for 24 h at 25 °C followed by an oven post-cure at 80 °C for 4 h. Test samples of 3DAWC were cut by water jet along the longitudinal and transverse directions of the composite plate. The longitudinal direction of the samples was aligned with the warp tows. The size (length × width × thickness) of each 3DAWC sample was 120 × 18.7 × 4 mm, and the fiber volume fraction of the 3DAWC was approximately 55%. The surface and cross-section of a sample are shown in Fig. 2, and the material parameters of the glass-fiber tows and resin are listed in Table 2.

2.2. Quasi-static tension and tension–tension fatigue tests

The quasi-static tension and tension–tension fatigue tests were conducted on an INSTRON 8501 system at a cross-head speed of 1 mm min^{-1}. To monitor damage during the fatigue tests, an AE system (Physical Acoustics PCI-2) was employed. Two 300 kHz resonance transducers (Micro 30) were placed on the loading fixtures to determine when and where damage events took place. The sensors were attached to model 2/4/6 preamps providing 40 dB of gain and band-pass filtering of 200–400 kHz. The location of the AE source in the specimen was determined using a linear location method, and only the events recorded between the sensors were used to analyze the AE results. A threshold level of 50 dB was used to filter out the interference caused by the hydraulics. The tests

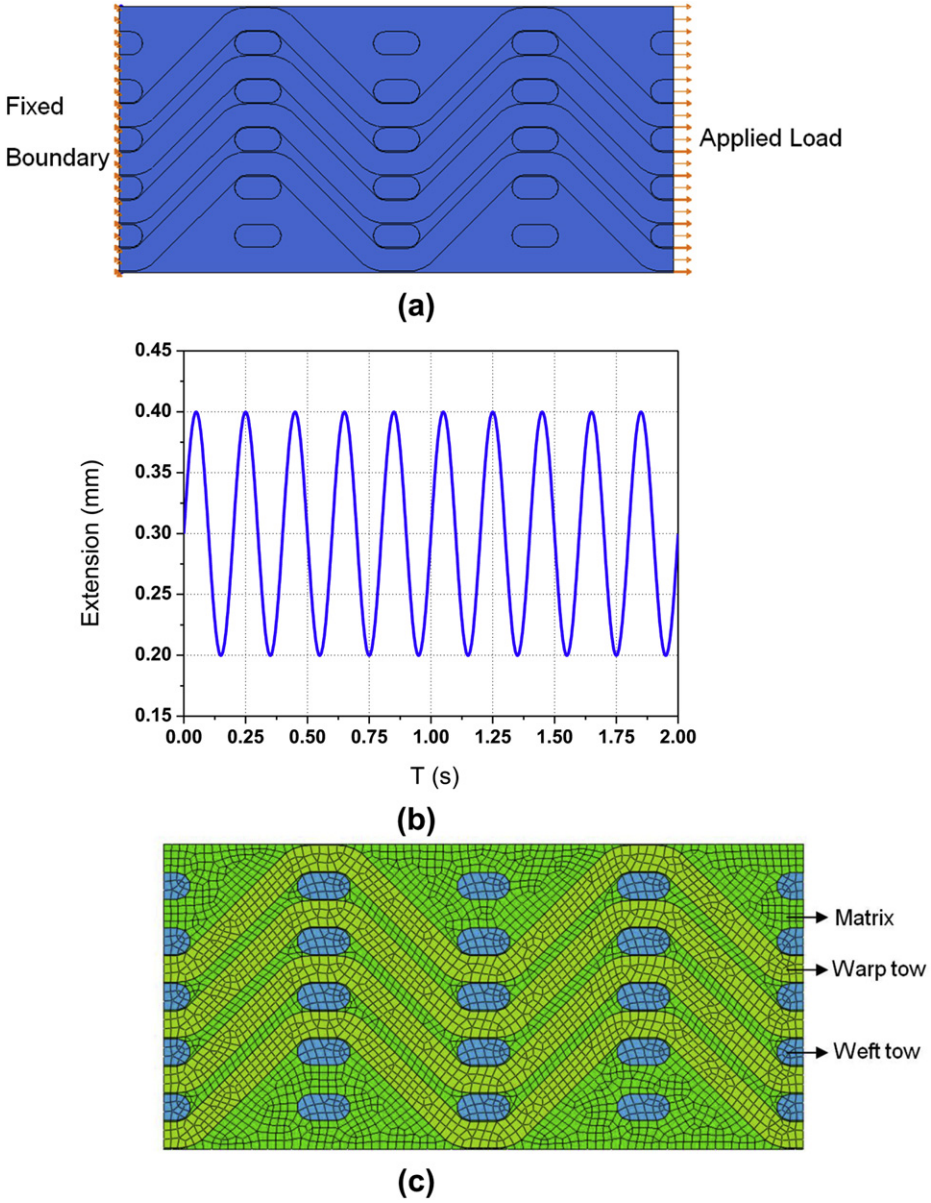

Fig. 3. Finite element model of the 3DAWC under tension–tension cyclic loading. (a) Micro-structural model of the 3DAWC; (b) displacement–control cyclic loading condition; (c) mesh scheme with the technique of coincidence of nodes.

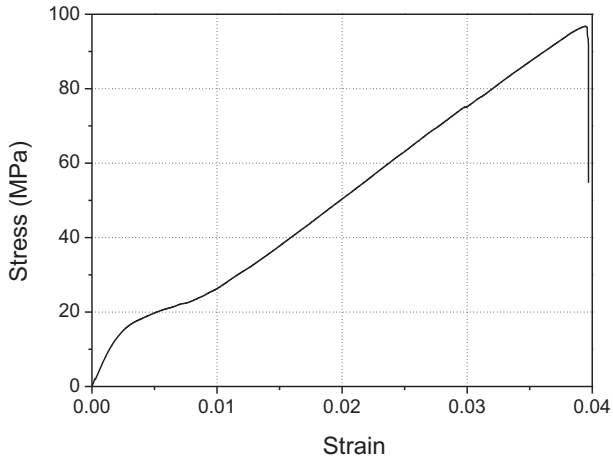

Fig. 4. Stress–strain curve under quasi-static tension.

were conducted under the sinusoidal wave-form cyclic loading with the frequency of 5 Hz and the stress ratio R (the ratio of the minimum stress to the maximum stress in one cycle) of 0.1. Three stress levels $\sigma_{max}/\sigma_{ult}$ (the ratio of the applied maximum stress in one cycle to the ultimate quasi-static tensile stress of the composite sample), i.e., 40%, 50% and 60%, were selected for the fatigue tests.

3. Finite element analyses

Finite element analysis (FEA) was employed to determine the stress distribution and regions of stress concentrations in the 3DAWC structure undergoing tension–tension cyclic loading. The finite element simulation was conducted using commercial finite element software (ABAQUS/Standard ver. 6.10).

As shown in Fig. 3a, a fiber tow-matrix 2-D model of the 3DAWC was created under tension-tension fatigue cyclic loading. The interaction between the resin and the fiber tows was defined as

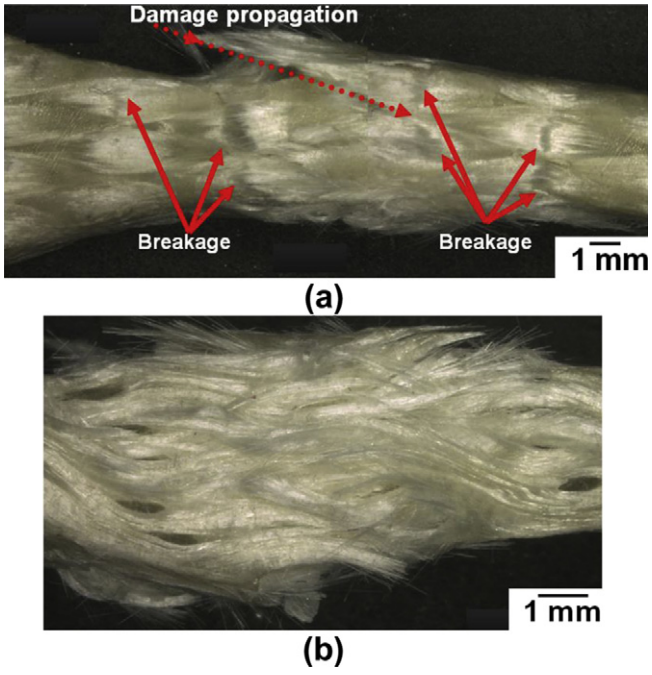

Fig. 5. Failure morphologies under quasi-static tension. (a) Surface showing fiber tow breakage; (b) cross-section showing fiber tow breakage and tow pullout.

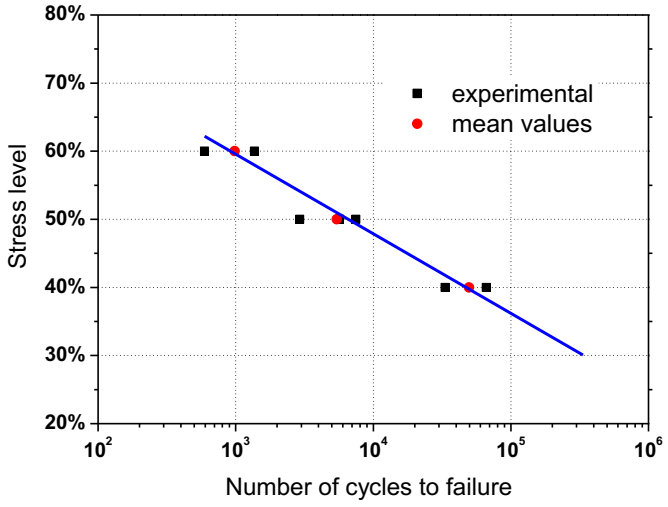

Fig. 6. S–N curve.

"SURFACE TO SURFACE CONTACT" with the "BONDING" condition of limit bonding to slave nodes set in tows. The resin surface was set as the master surface, and the tows were the slave surfaces. The loading and boundary conditions are presented in Fig. 3b, where displacement-control cyclic loading was applied at the right end of

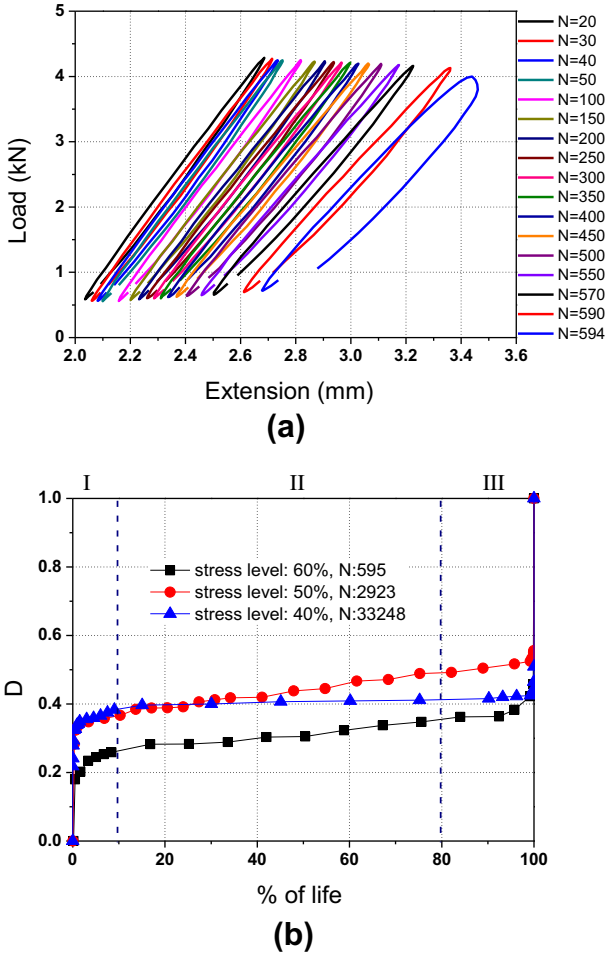

Fig. 7. Mechanical degradation curves. (a) Load–extension hysteresis loops (stress level: 60%, number of cycles to failure: 595); (b) damage index as a function of percentage of life.

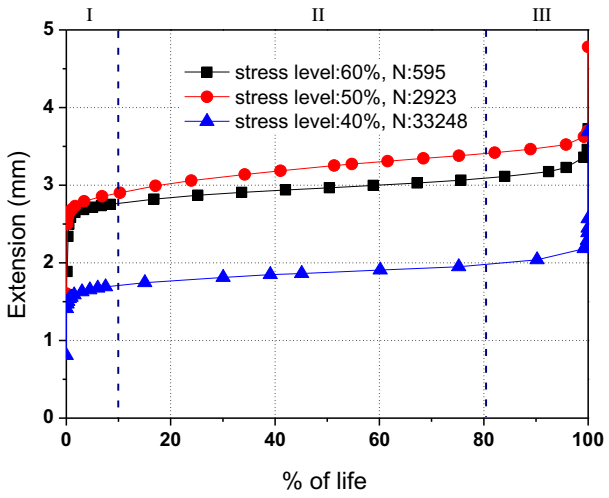

Fig. 8. Comparisons of maximum extension curves for three stress levels.

the 3DAWC, and the left end was fixed. As shown in Fig. 3c, each component of the 3DAWC was meshed with a coincidence of nodes technique. The element type was CPS4R Quad-dominated, and the element numbers of the resin, warp tows and weft tows were 1835, 1556 and 485, respectively.

4. Results and discussions

4.1. Mechanical behavior under quasi-static tensile and fatigue tests

Stress–Strain curve. Quasi-static tensile tests were performed on the 3DAWC samples, and a typical stress–strain curve is presented in Fig. 4. The maximum load and extension were 7235.68 N and 4.77 mm, respectively. The ultimate failure morphologies are presented in Fig. 5. The primary damage modes are breakages of the undulated warp tows and subsequent tows pullout, indicating that the warp tows carried most of the load during the static tensile loading. Moreover, the damage initiated from the edge of the sample, then propagated towards the center.

S–N, load–extension and damage index curves. The S–N curve of the 3DAWC under three different stress levels (40%, 50% and 60% of static strength) is shown in Fig. 6. The curve plots magnitude of the cyclic stress level versus the number of cycles to failure, and shows that the number of cycles to failure decreased as the applied stress level increased.

To evaluate the progression of damage during fatigue loading, Load-Extension curves for selected cycles during the fatigue test are shown in Fig. 7a. As the number of cycles increases, extension also increases, despite a constant load cycle. The behavior is attributed to progressive and cumulative fatigue damage. Simultaneously, the enveloped area of each cyclic loop increased as the fatigue test proceeded, indicating an increase in damage, and increased energy dissipation within the composite.

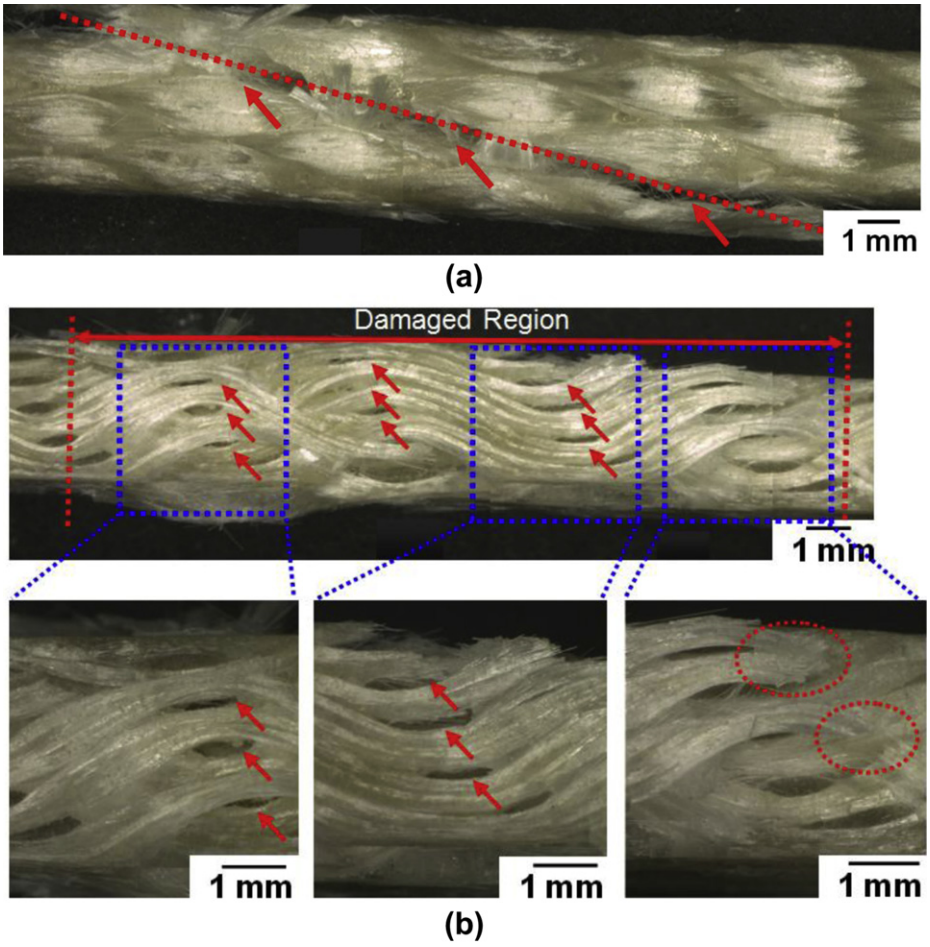

Fig. 9. Typical fatigue failure modes (stress level: 60%, number of cycles to failure: 595). (a) Surface showing resin damage and fiber tow breakage; (b) cross-section showing interface debonding and fiber tow breakage.

Damage index curves are shown in Fig. 7b to illustrate the mechanical degradation of the 3DAWC. The damage index (D) is defined in terms of the elastic modulus, as presented in Eq. (1) [18].

$$D = 1 - \frac{E}{E_0} \tag{1}$$

where E is the elastic modulus of the material during fatigue test, E_0 is the elastic modulus of the material before the fatigue test. When the test begins, $E = E_0$ and when the test ends, $E = 0$. Thus, D values range between 0 and 1.

The fatigue behavior shown in Fig. 7b, exhibits three stages. Stages I and III features sharp increases in D, although both stages represent a short portion of the fatigue life. In contrast, Stage II corresponds to a gradual and steady increase in D. Stage II represents a majority of the fatigue life, during which the 3DAWC material steadily accumulates fatigue damage.

Maximum extension curves. The maximum extension curves under various stress levels are plotted, as shown in Fig. 8. It shows a plot of extension versus percentage of fatigue life. The extension trend also shows three stages – a sharp increase in Stages I and III, both of which corresponding to a relatively short portion of the fatigue life, and a steady and gradual increase in Stage II, which consumes the majority of the fatigue life. Thus, the mechanical performance of the 3DAWC degrades gradually during the process of fatigue damage, as the dominant failure mechanisms (summarized in Section 4.5) evolve during Stages I, II and III.

4.2. Ultimate fatigue failure modes

Fig. 9 shows the typical fatigue damage modes of the 3DAWC viewed from the surface (edge) and in cross-section. Resin cracking, tows breakages and resin–tow interface debonding are the primary damage modes during tension–tension fatigue. In particular, resin cracks and tows breakages are evident in the edge view, and

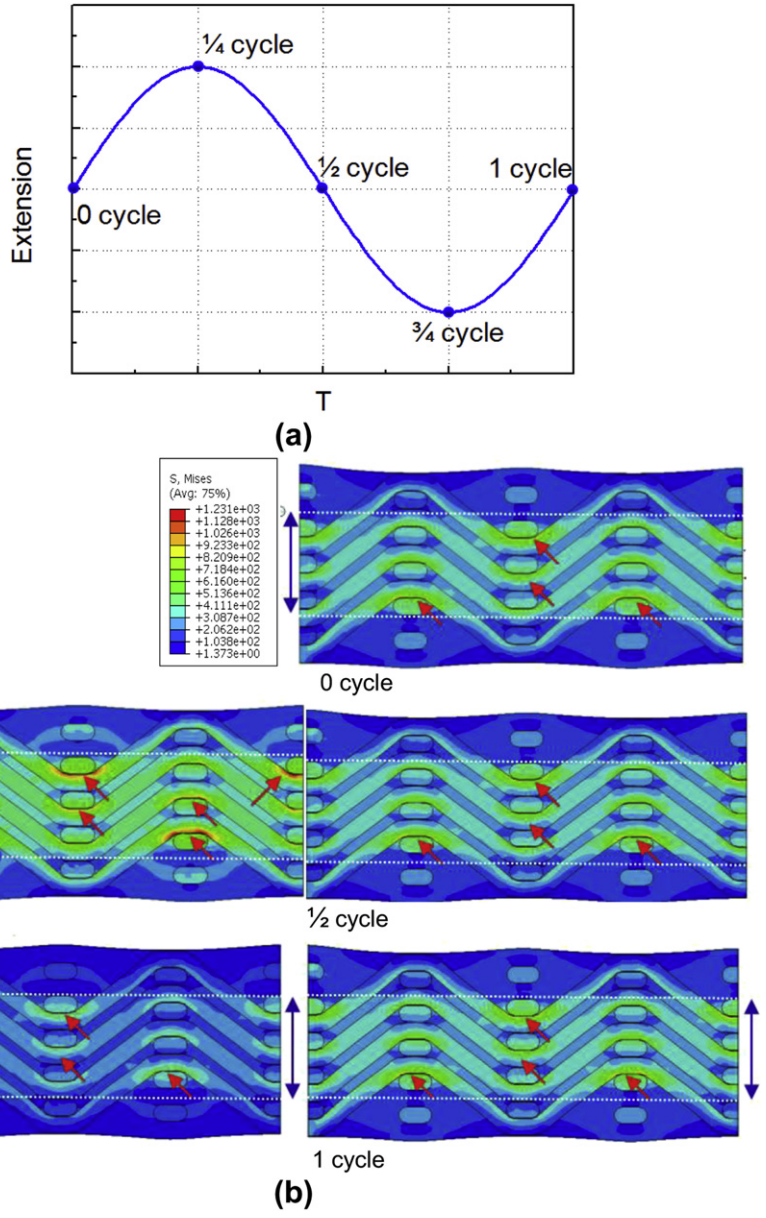

Fig. 10. (a) Special time points in a single load cycle; (b) stress distribution and stress concentration regions in the 3DAWC structure.

interface debonding is apparent in the cross-sectional view. Damage initiated at the edge of the sample, then propagated to the inner regions along the direction shown in Fig. 9a. Because the undulated warp tows carried the majority of the load during the fatigue test, debonding occurred most frequently at regions of concentrated stress that arose at warp tow–resin–weft tow interfaces. At these sites, the undulated warp tows showed the maximum amplitude of undulation, as shown in Fig. 9b. Therefore, the damage modes exhibited in quasi-static tension (see Fig. 5) and tension–tension fatigue differ significantly. Fiber tow breakage plays an important role in the damage incurred during quasi-static tensile loading, while tow cracking, interface debonding and fiber tow breakage characterize the damage during tension–tension cyclic loading.

4.3. Stress distribution

Fig. 10 shows contour images of the stress distribution during a single tension–tension load cycle. These images show that the inner central region (as indicated between the two white dashed lines) of the 3DAWC carry the majority of the applied load during the load cycle. This inner central region occupies the highest volume content of fiber tows, and the stress concentrations occur at the regions marked by red arrows, where the maximum curvature occurs and the weft tows cross the warp tows. These highly stressed sites are also sites of interface debonding, as shown in the images in Fig. 9. Along the load-carrying direction, the system of undulated warp tows is the primary load-carrying component, unlike the weft tows which are perpendicular to the loading direction.

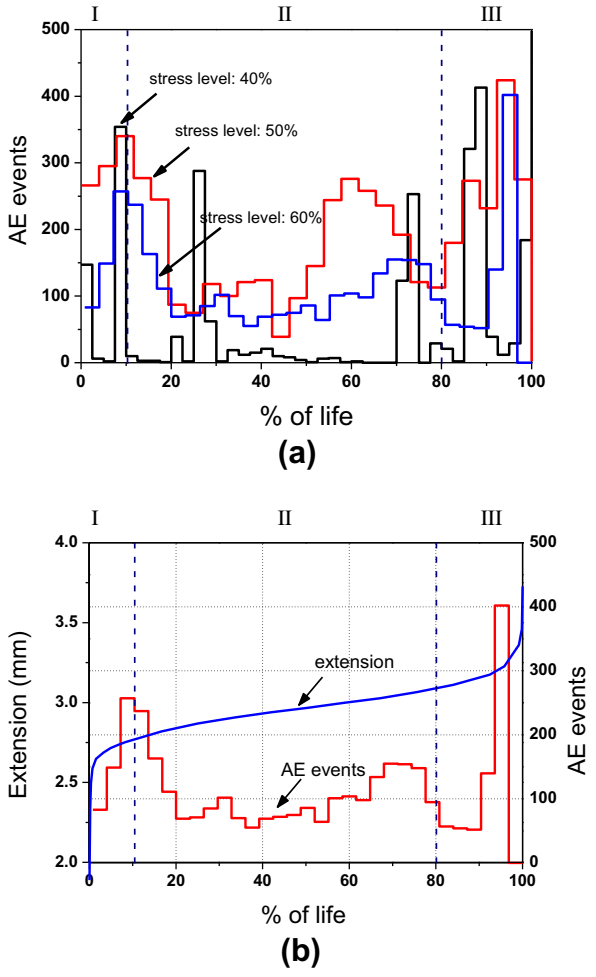

Fig. 11. Three stages in tension–tension fatigue. (a) Comparisons of AE events vs. percentage of life curves for three stress levels; (b) curves of maximum extension and AE events as a function of percentage of life (stress level: 60%, number of cycles to failure: 595).

4.4. Fatigue damage modes at specific points of percentage of life

The cumulative damage during tension–tension cyclic loading is summarized in the plots of AE events as a function of percentage of life for three stress levels, as shown in Fig. 11a. The data sets for each of the three stress levels exhibit three peaks in number of AE events at roughly 10%, 80% and 90% life. The peaks divide the fatigue life into three stages that correspond to three intervals of fatigue life,

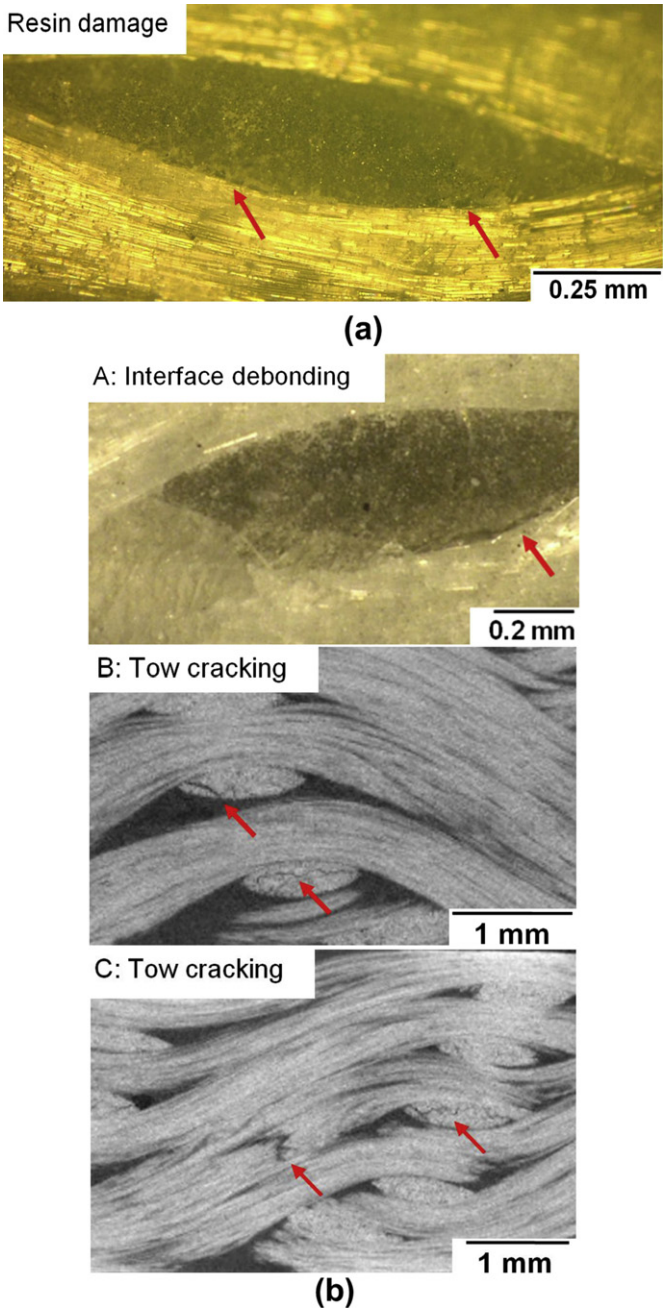

Fig. 12. Fatigue damage modes at specific points of percentage of life. (a) Approximately 10% of life, showing resin damage; (b) approximately 80% of life, showing interface debonding and tow cracking.

i.e., 0–10%, 10–80% and 80%–100%. The three stages are more apparent when combing the curves of maximum extension and AE events as a function of percentage of life, as shown in Fig. 11b. Each stage includes one peak in AE events, corresponding to a transition to a different stage and possibly a different fatigue damage mode.

To investigate and determine the dominant damage mode during each stage, two fatigue tests under the stress level of 50% were interrupted to examine the microstructures. Using the AE data to monitor fatigue damage in real time, tests were interrupted at the first and second peaks of AE event numbers corresponding to roughly 10% and 80% of fatigue life. Micro-structural damage was investigated by inspecting polished sections and by non-destructive evaluation using X-ray computed tomography (micro-CT). Fig. 12a shows a sample after approximately 10% of life, that exhibits only resin damage at regions of stress concentration (see arrow), as described in Section 4.3. In contrast, after 80% fatigue life, sample shows resin damage at the regions of stress concentrations, interface debonding between tows and resin, and tows breakages, as shown in Fig. 12b. Thus, damage is confined to the matrix during the first stage of fatigue, while damage during Stage II occurs by interface debonding and tows breakages.

4.5. Fatigue damage mechanisms

Tension–tension fatigue damage mechanisms of 3DAWC composites can be divided into three stages. During the first stage, resin damage occurred at stress concentration regions after a small number of cycles. This stage, corresponding to the initial 10% of fatigue life, resulted in an abrupt degradation of mechanical performance of the composite which led to a sharp increase of extension.

As fatigue progressed, matrix cracking gradually propagated into regions adjacent to stress concentrations until the second stage was reached. As the number of cycles increased, interface debonding initiated at regions of stress concentrations, causing interface cracking, which occurred continuously from approximately 10–60% of life and was the dominant damage mode during this period. During Stage II, tows breakage occurred from approximately 60–80% of life and was the dominant damage mode. Stage II involved a large number of cycles corresponding to approximately 70% of fatigue life, causing continuous gradual degradation of mechanical properties.

During the third stage, which corresponded to the last ~20% of fatigue life, cumulative tows breakages caused extensive load shedding, leading rapidly to the ultimate fatigue failure of the composite. This stage occupied a relatively short portion of the fatigue life and corresponded to a sharp increase in extension.

5. Conclusions

An experimental investigation of the tension–tension fatigue behavior of a layer-to-layer 3DAWC was performed. The objective was to understand the response of the 3DAWC architecture under tension–tension fatigue conditions and the corresponding damage modes. The damage index and extension curves showed gradual degradation in load-bearing ability in three distinct stages during fatigue loading. AE detection and interrupted tests were used to characterize the three stages of progressive fatigue damage, and each stage showed specific fatigue damage modes. Stage I (initial 10% of fatigue life) was characterized by rapid damage accumulation, while Stage II (10–80% of fatigue life) featured a more gradual and steady increase in damage, and Stage III (80–100% of fatigue life) showed rapid damage accumulation and catastrophic failure. The primary damage mechanisms included matrix cracking during Stage I, interface debonding and tow cracking during Stage II, and tow breakage during Stage III. The progression of damage showed dependence on both applied stress level (i.e., loading magnitude) and duration of applied load.

An issue of critical importance involves the effect of stress concentrations on long-term durability and the evolution of fatigue damage. For 3DAWC materials, fatigue behavior is sensitive to fiber architecture, as both the experimental and micro-structural FEA results indicate that stress concentrations arise at regions of maximum tow curvature where weft tows cross warp tows. These highly stressed nodes are sites of matrix damage initiation (Stage I) and interface debonding (Stage II). Along the load-carrying direction, the system of undulating warp tows is the primary load-carrying component, while the weft tows are loaded transversely. The 3DAWC are designed primarily to improve through-thickness properties and high resistance to delamination. However the results shown here indicate that fabric architecture strongly affects crack initiation and growth under tension-tension fatigue conditions.

Better understanding of fatigue damage mechanisms will guide the design of future 3DAWC materials with improved fatigue resistance and damage tolerance. The fiber and matrix type and the various woven architectures will affect fatigue resistance, and future research with new woven architectures will provide improved understanding of the tradeoffs and limitations involved. The analysis shown here indicates that the fatigue resistance of 3DAWC materials may be improved by using woven architectures that reduce stress concentrations at warp tow cross-over regions. However, these same warp tow cross-over regions produce high interlaminar shear strength in the 3DAWC. Thus, improvements in fatigue resistance may very well involve tradeoffs between interlaminar shear properties and tensile fatigue resistance.

Acknowledgements

The authors acknowledge the financial supports from the National Science Foundation of China (Grant Number 11272087). The financial supports from Foundation for the Author of National Excellent Doctoral Dissertation of PR China (FANEDD, No. 201056), Shanghai Rising-Star Program (11QH1400100) and the Fundamental Research Funds for the Central Universities of China are also gratefully acknowledged.

The authors also acknowledge Yinghui Hu and Rohan Panikar for their advice and support, and Anitha Krishnan and Dagliyan Grant from USC Molecular Imaging Center for their kind help on composites damage scanning using micro-CT.

References

[1] A.P. Mouritz, M.K. Bannisterb, P.J. Falzonb, K.H. Leongb, Comp. Part A 30 (12) (1999) 1445.
[2] S.Z. Sheng, S.V. Hoa, J. Thermoplast. Comp. Mater. 16 (1) (2003) 45.
[3] X. Chen, M. Spola, J. Gisbert Paya, P. Mollst Sellabona, J. Tex. I 90 (1) (1999) 91.
[4] X. Chen, P. Potiyaraj, Tex. Res. J. 69 (9) (1999) 648.
[5] B.Z. Sun, B.H. Gu, X. Ding, Polym. Test. 24 (4) (2005) 447.
[6] B.Z. Sun, B.H. Gu, J. Comp. Mater. 41 (24) (2007) 2915.
[7] P. Lapeyronnie, P.L. Grognec, C. Binétruy, F. Boussu, Comp. Struct. 93 (11) (2011) 2795.
[8] W.F. Dong, J. Xiao, Y. Li, Mater. Sci. Eng. A 457 (1, 2) (2011) 199.
[9] P. Tan, L.Y. Tong, G.P. Steven, Comp. Part A 30 (5) (1999) 637.
[10] S. Nehme, A. Hallal, F. Fardoun, et al., J. Comp. Mater. 45 (16) (2011) 1699.
[11] A. Hallal, R. Younes, S. Nehme, F. Fardoun, J. Comp. Mater. 45 (17) (2011) 1793.
[12] F. Cui, B.Z. Sun, B.H. Gu, J. Comp. Mater. 45 (14) (2010) 1499.
[13] Z.J. Li, B.Z. Sun, B.H. Gu, Comput. Mater. Sci. 49 (1) (2010) 171.
[14] Y.Y. Tang, B.Z. Sun, B.H. Gu, Int. J. Damage Mech. 20 (3) (2010) 323.
[15] K.H. Tsai, C.H. Chiu, T.H. Wu, Comp. Sci. Technol. 60 (2) (2000) 241.
[16] Y. Gowayed, H. Fan, Polym. Comp. 22 (6) (2001) 762.
[17] L.M. Jin, B.Z. Sun, B.H. Gu, J. Comp. Mater. 46 (8) (2012) 883.
[18] L. Lemaitre, J.L. Chaboche, Mechanics of Solid Materials, Cambridge University Press, London, 1990.